Development of a fan-beam TDLAS-based tomographic sensor for rapid imaging of temperature and gas concentration

Citation for published version:
Liu, C, Xu, L, Chen, J, Cao, Z, Lin, Y & Cai, W 2015, 'Development of a fan-beam TDLAS-based tomographic sensor for rapid imaging of temperature and gas concentration' Optics Express, vol. 23, no. 17, pp. 22494-22511.

Published In:
Optics Express

Development of a fan-beam TDLAS-based tomographic sensor for rapid imaging of temperature and gas concentration

Chang Liu,[1,2] Lijun Xu,[1,2,*] Jianliang Chen,[1,2] Zhang Cao,[1,2] Yuzhen Lin,[3] and Weiwei Cai[4]

[1] *Ministry of Education's Key Laboratory of Precision Opto-mechatronics Technology, Beijing, 100191, China*
[2] *School of Instrument Science and Opto-Electronic Engineering, Beihang University, Beijing, 100191, China*
[3] *School of Energy and Power Engineering, Beihang University, Beijing, 100191, China*
[4]*Department of Chemical Engineering and Biotechnology, University of Cambridge, Cambridge CB2 3RA, United Kingdom*
[*] *lijunxu@buaa.edu.cn*

Abstract: This work aims to develop a fan-beam tomographic sensor using tunable diode lasers that can simultaneously image temperature and gas concentration with both high spatial and temporal resolutions. The sensor features three key advantages. First, the sensor bases on a stationary fan-beam arrangement, by which a high spatial resolution is guaranteed because the distance between two neighboring detectors in a view is approximately reduced to the size of a photodiode. Second, fan-beam illumination from five views is simultaneously generated instead of rotating either the fanned beams or the target, which significantly enhances the temporal resolution. Third, a novel set of optics with the combination of anamorphic prism pair and cylindrical lens is designed, which greatly improves the uniformity of the planar beams, and hence improves the reconstruction fidelity. This paper reports the tomographic model, optics design, numerical simulation and experimental validation of the sensor. The sensor exhibits good applicability for flame monitoring and combustion diagnosis.

OCIS codes: (300.1030) Absorption; (300.0300) Spectroscopy; (100.6950) Tomographic image processing; (280.1740) Combustion diagnostics.

References and links

1. M. A. Bolshov, Y. A. Kuritsyn, and Y. V. Romanovskii, "Tunable diode laser spectroscopy as a technique for combustion diagnostics," Spectrochim. Acta B At. Spectrosc. **106**, 45–66 (2015).
2. M. Lackner, "Tunable diode laser absorption spectroscopy (TDLAS) in the process industries - A review," Rev. Chem. Eng. **23**(2), 65–147 (2007).
3. R. Sur, K. Sun, J. Jeffries, R. Hanson, R. Pummill, T. Waind, D. Wagner, and K. Whitty, "TDLAS-based sensors for in situ measurement of syngas composition in a pressurized, oxygen-blown, entrained flow coal gasifier," Appl. Phys. B **116**(1), 33–42 (2014).
4. F. Li, X. Yu, H. Gu, Z. Li, Y. Zhao, L. Ma, L. Chen, and X. Chang, "Simultaneous measurements of multiple flow parameters for scramjet characterization using tunable diode-laser sensors," Appl. Opt. **50**(36), 6697–6707 (2011).
5. O. Witzel, A. Klein, C. Meffert, S. Wagner, S. Kaiser, C. Schulz, and V. Ebert, "VCSEL-based, high-speed, in situ TDLAS for in-cylinder water vapor measurements in IC engines," Opt. Express **21**(17), 19951–19965 (2013).
6. X. Liu, J. B. Jeffries, and R. K. Hanson, "Measurement of Nonuniform Temperature Distributions Using Line-of-Sight Absorption Spectroscopy," AIAA J. **45**(2), 411–419 (2007).
7. C. Liu, L. Xu, and Z. Cao, "Measurement of nonuniform temperature and concentration distributions by combiningline-of-sight TDLAS with regularization methods," Appl. Opt. **52**(20), 4827–4842 (2013).
8. M. P. Wood and K. B. Ozanyan, "Simultaneous temperature, concentration, and pressure imaging of water vapor in a turbine engine," IEEE Sens. J. **15**(1), 545–551 (2015).

#240260 Received 4 May 2015; revised 10 Aug 2015; accepted 14 Aug 2015; published 18 Aug 2015

9. P. Wright, N. Terzija, J. L. Davidson, S. Garcia-Castillo, C. Garcia-Stewart, S. Pegrum, S. Colbourne, P. Turner, S. D. Crossley, T. Litt, S. Murray, K. B. Ozanyan, and H. McCann, “High-speed chemical species tomography in a multi-cylinder automotive engine,” Chem. Eng. J. **158**(1), 2–10 (2010).
10. M. G. Twynstra and K. J. Daun, “Laser-absorption tomography beam arrangement optimization using resolution matrices,” Appl. Opt. **51**(29), 7059–7068 (2012).
11. N. Terzija, J. L. Davidson, C. A. Garcia-Stewart, P. Wright, K. B. Ozanyan, S. Pegrum, T. J. Litt, and H. McCann, “Image optimization for chemical species tomography with an irregular and sparse beam array,” Meas. Sci. Technol. **19**(9), 094007 (2008).
12. W. Cai and C. F. Kaminski, “A tomographic technique for the simultaneous imaging of temperature, chemical species, and pressure in reactive flows using absorption spectroscopy with frequency-agile lasers,” Appl. Phys. Lett. **104**(3), 034101 (2014).
13. L. Ma, X. Li, S. T. Sanders, A. W. Caswell, S. Roy, D. H. Plemmons, and J. R. Gord, “50-kHz-rate 2D imaging of temperature and H2O concentration at the exhaust plane of a J85 engine using hyperspectral tomography,” Opt. Express **21**(1), 1152–1162 (2013).
14. L. Ma, W. Cai, A. W. Caswell, T. Kraetschmer, S. T. Sanders, S. Roy, and J. R. Gord, “Tomographic imaging of temperature and chemical species based on hyperspectral absorption spectroscopy,” Opt. Express **17**(10), 8602–8613 (2009).
15. R. M. Spearrin, C. S. Goldenstein, I. A. Schultz, J. B. Jeffries, and R. K. Hanson, “Simultaneous sensing of temperature, CO, and CO_2 in a scramjet combustor using quantum cascade laser absorption spectroscopy,” Appl. Phys. B **117**(2), 689–698 (2014).
16. J. Song, Y. Hong, G. Wang, and H. Pan, “Algebraic tomographic reconstruction of two-dimensional gas temperature based on tunable diode laser absorption spectroscopy,” Appl. Phys. B **112**(4), 529–537 (2013).
17. F. Wang, K. F. Cen, N. Li, J. B. Jeffries, Q. X. Huang, J. H. Yan, and Y. Chi, “Two-dimensional tomography for gas concentration and temperature distributions based on tunable diode laser absorption spectroscopy,” Meas. Sci. Technol. **21**(4), 045301 (2010).
18. V. Kasyutich and P. Martin, “Towards a two-dimensional concentration and temperature laser absorption tomography sensor system,” Appl. Phys. B **102**(1), 149–162 (2011).
19. R. Villarreal and P. L. Varghese, “Frequency-resolved absorption tomography with tunable diode lasers,” Appl. Opt. **44**(31), 6786–6795 (2005).
20. E. J. Beiting, “Fiber-optic fan-beam absorption tomography,” Appl. Opt. **31**(9), 1328–1343 (1992).
21. F. P. Hindle, S. J. Carey, K. Ozanyan, D. E. Winterbone, E. Clough, and H. McCann, “Measurement of gaseous hydrocarbon distribution by a near-infrared absorption tomography system,” J. Electron. Imaging **10**(3), 593–600 (2001).
22. S. Shakya, P. Munshi, A. Luke, and D. Mewes, “Computerized tomography application in oil industry using KT-2 signature,” Res. Nondestr. Eval. **26**(2), 61–89 (2015).
23. M. Buchmann and D. Mewes, “Tomographic Measurement and Reconstruction Techniques,” in *Optical Measurements*, F. Mayinger and O. Feldmann eds. (Springer Berlin Heidelberg, 2001), pp. 301–339.
24. L. Xu, T. Wei, J. Zhou, and Z. Cao, “Modified Landweber algorithm for robust particle sizing by using Fraunhofer diffraction,” Appl. Opt. **53**(27), 6185–6193 (2014).
25. W. Q. Yang, D. M. Spink, T. A. York, and H. McCann, “An image-reconstruction algorithm based on Landweber’s iteration method for electrical-capacitance tomography,” Meas. Sci. Technol. **10**(11), 1065–1069 (1999).
26. L. Xu, C. Liu, D. Zheng, Z. Cao, and W. Cai, “Digital signal processor-based high-precision on-line Voigt lineshape fitting for direct absorption spectroscopy,” Rev. Sci. Instrum. **85**(12), 123108 (2014).
27. C. Liu, L. Xu, Z. Cao, and H. McCann, “Reconstruction of axisymmetric temperature and gas concentration distributions by combining fan-beam TDLAS with onion-peeling deconvolution,” IEEE Trans. Instrum. Meas. **63**(12), 3067–3075 (2014).
28. S. A. Tsekenis, N. Tait, and H. McCann, “Spatially resolved and observer-free experimental quantification of spatial resolution in tomographic images,” Rev. Sci. Instrum. **86**(3), 035104 (2015).
29. D. Verhoeven, “Limited-data computed tomography algorithms for the physical sciences,” Appl. Opt. **32**(20), 3736–3754 (1993).
30. M. Beister, D. Kolditz, and W. A. Kalender, “Iterative reconstruction methods in X-ray CT,” Phys. Med. **28**(2), 94–108 (2012).
31. C. Liu, L. Xu, F. Li, Z. Cao, S. Tsekenis, and H. McCann, “Resolution-doubled one-dimensional wavelength modulation spectroscopy tomography for flame flatness validation of a flat-flame burner,” Appl. Phys. B **120**(3), 407-416 (2015).

---

1. Introduction

Over the past decades, tunable diode laser absorption spectroscopy (TDLAS) has been widely used for combustion diagnosis due to its fast response, high sensitivity, and non-invasiveness [1–5]. However, the traditional line-of-sight (LOS) TDLAS technique is constrained to retrieve the path-averaged temperature and gas concentration. For some applications, it is necessary to rapidly and accurately obtain the distributions of temperature and gas

#240260 Received 4 May 2015; revised 10 Aug 2015; accepted 14 Aug 2015; published 18 Aug 2015

concentrations. By obtaining absorption signals at multiple transitions, the probability density function of temperature along the laser path can be inferred by assuming a constant gas concentration [6]. Furthermore, the resolution of non-uniformities along the laser path was also demonstrated in our previous work by considering the *a priori* information, i.e., temperature variation tendency [7]. However, the above attempts were only limited to one-dimensional spatial resolution.

By combining TDLAS with the tomographic concept, two-dimensional spatial resolution of the temperature and gas concentration can be enabled. The spatial resolution of TDLAS-based tomography is majorly determined by both the intensiveness (# of projections or # of transitions sampled) and effectiveness (beam arrangement) of the tomographic sampling. For the measurements with limited optical access, the beam arrangement should be optimized to achieve sufficient resolution required by the applications [8–11]. Furthermore, the so-called frequency-agile tomography (FAT) seeks to increase the spectral sampling [12–14] through broadband wavelength sweeping so that the deficiencies in spatial sampling can be alleviated and intermediate spatial resolution can be obtained. However, compared with TDLAS-based tomography, the FAT technique requires an expensive broadband light source such as the supercontinuum radiation [12], Fourier-domain mode-locked (FDML) laser [13], or quantum cascade laser source [15]. For the target with sufficient optical access, e.g. the exhaust of an engine or a combustion chamber, the spatial resolution can be improved by simply increasing both the number of views and laser beams [16–20]. The previous implementations rely on mechanical mechanisms to either rotate the probing beams or translate the target. For instance, Wang *et al* captured the absorption signals by simultaneously rotating four laser beams on the rotating platforms [17]; Kasyutich *et al* acquired the projections from different views by rotating the laser source and the photodiode on two moveable carriages along a circular rail [18]; and Villarreal *et al* obtained the tomographic image of the flat flame by moving the burner on a translation stage [19]. However, the mechanical movements inevitably undermine the temporal resolution which is also crucial for the monitoring of high speed flows such as the exhaust of a scramjet.

This work aims to design a TDLAS-based tomographic sensor with both high spatial and temporal resolutions for rapid imaging of temperature and gas concentration with a stationary fan-beam arrangement instead of a parallel-beam arrangement. In a parallel-beam arrangement, a set of optics that contains a collimator and a detector is used to obtain one ray measurement [21]. In this way, the spatial resolution of the tomographic image is limited by the size of the collimators which is larger than that of a detector. When adopting the fan-beam arrangement, however, the projections of the fan-beam illumination in a view can be obtained using one source and multiple detectors [22,23]. The distance between two neighboring detectors can be reduced to about the size of a photodiode, which contributes to greatly improving the spatial resolution. To achieve this, a novel set of optics with the combination of anamorphic prism pair and cylindrical lens is designed, which significantly improves the uniformity of the fan-shaped planar illumination, and hence improving the reconstruction fidelity. Furthermore, fan-beam illumination from five views is simultaneously generated, by which the temporal resolution of the tomographic sensor can be greatly increased. The remainder of the paper is organized as follows: section 2 provides both the background of TDLAS and the mathematical formulation of the tomographic problems; section 3 details the sensor implementation; and section 4 presents results of both the numerical validation and experimental demonstration with the final section summarizing the paper.

2. Theoretical background

To facilitate discussion of the fan-beam TDLAS-based tomographic sensor, this section provides a brief summary of the fundamentals of TDLAS and tomography. According to the Beer's law, when a collimated laser beam at a of frequency v [cm^{-1}] enters a flame with a thickness of L [cm], the absorbance α_v is expressed as

#240260 Received 4 May 2015; revised 10 Aug 2015; accepted 14 Aug 2015; published 18 Aug 2015

$$\alpha_v = \int_0^L P(x)X(x)S[T(x)]\phi dl, \tag{1}$$

where $P(x)$ [atm] is the local total pressure, $X(x)$ the local molar fraction of the absorbing species (noted as gas concentration hereafter), $T(x)$ [K] the local temperature, ϕ [cm] the line-shape function. The line strength of transition $S[T(x)]$ [cm^{-2}atm^{-1}] is a function of temperature as follows:

$$S(T) = S(T_0)\frac{Q(T_0)}{Q(T)}\left(\frac{T_0}{T}\right)\exp\left[-\frac{hcE''}{k}\left(\frac{1}{T}-\frac{1}{T_0}\right)\right]\times\frac{1-\exp\left(-hcv_0/kT\right)}{1-\exp\left(-hcv_0/kT_0\right)}, \tag{2}$$

where h [J·s] is Planck's constant, c [cm·s^{-1}] the speed of light, k [J·K^{-1}] the Boltzmann's constant, $Q(T)$ the partition function of the absorbing molecule, T_0 [K] the reference temperature, v_0 [cm^{-1}] the line-center frequency, and E" [cm^{-1}] the lower energy of the transition. Because the line-shape function ϕ is normalized so that $\int_{-\infty}^{+\infty}\phi dv \equiv 1$, integrated absorbance A_v of the transition can be inferred from Eq. (1) as

$$A_v = \int_{-\infty}^{\infty}\alpha_v dv = \int_0^L P(x)X_{abs}(x)S[T(x)]dl. \tag{3}$$

For the tomographic analysis, the circular region of interest (ROI) is discretized into N (= 332 in this case) grids, as shown in Fig. 1. Given that the radius of the ROI is 3 cm, a spacing of 0.3 cm between the neighboring grids along both the directions of x- and y-axes is obtained. In each grid, the flame parameters such as pressure, temperature and gas concentration are assumed to be constant. Each fan-beam illumination penetrates the ROI and is picked up by an array of 12 equal-spaced photodiodes. Therefore, the fan-beam illumination is equivalent to 12 laser beams in a fan-shaped arrangement. The distance between the neighboring photodiodes is denoted as d. The fan-beam illumination from five views produces a total of M (= 60 in this case) projections, i.e., the integrated absorbances. It should be noted that the numbers of discretized grids, views and laser beams in each view are chosen in consideration of both accuracy of the tomographic image and complexity of the optics, which will be detailed in section 4.

According to Eq. (3), the sampled integrated absorbance $A_{v,i}$ obtained from the i-th laser beam can be expressed as

$$A_{v,i} = \sum_{j=1}^{N} a_{v,j}L_{ij} = \sum_{j=1}^{N}[PS(T)X]_{v,j}L_{ij}, \tag{4}$$

where i and j are the indices of the laser beams and the grids, $a_{v,j}$ the density of the integrated absorbance in the j-th grid, L_{ij} the absorption path length of the i-th laser beam within the j-th grid. In general, Eq. (4) can be compactly rewritten as

$$\boldsymbol{L}\boldsymbol{a}_v = \boldsymbol{A}_v, \tag{5}$$

where the $M \times N$ matrix $\boldsymbol{L}$ is

$$\boldsymbol{L} = \begin{bmatrix} L_{11} & L_{12} & \cdots & L_{1N} \\ L_{21} & L_{22} & \cdots & L_{2N} \\ \vdots & \vdots & \ddots & \vdots \\ L_{M1} & L_{M2} & \cdots & L_{MN} \end{bmatrix}, \tag{6}$$

the column vector $\boldsymbol{a}_v = \{a_{v,1}, a_{v,2}, \ldots, a_{v,N},\}^T$ and $\boldsymbol{A}_v = \{A_{v,1}, A_{v,2}, \ldots, A_{v,M},\}^T$. Given the geometrical arrangement of the laser beams, $\boldsymbol{L}$ can be determined. In this work, $\boldsymbol{a}_v$ is retrieved

#240260 Received 4 May 2015; revised 10 Aug 2015; accepted 14 Aug 2015; published 18 Aug 2015

using a modified Landweber algorithm, by which a stable solution of the inverse problem can be obtained with a limited number of ray measurements [8,11,24,25]. By taking the gradient of the least-squares objective function $||\boldsymbol{L}\boldsymbol{a}_v\text{-}\boldsymbol{A}_v||^2$ with respect to $\boldsymbol{a}_v$, the modified Landweber algorithm is given in an iterative form as

$$\boldsymbol{a}_v^{k+1} = \boldsymbol{a}_v^k + \lambda_k \boldsymbol{L}^T(\boldsymbol{A}_v - \boldsymbol{L}\boldsymbol{a}_v^k), \tag{7}$$

where $\boldsymbol{a}_v^k$ is the reconstruction of the density of the integrated absorbance at the *k*-th iteration, λ_k the relaxation parameter that is determined using a "line search" strategy in each iteration. It is worth mentioning that the modified Landweber algorithm has been found robust in case of limited views and ray measurements. This algorithm not only offers generality but also has an advantageous feature of taking into account *a priori* information about the solution such as smoothness of the subject and value constraints in each iteration. In section 4, more details will be given on justification of the modified Landweber algorithm.

In general, the real distributions of temperature and gas concentration are quite smooth due to heat transfer and mass diffusion. Therefore, a Gaussian low-pass filter of size 3 × 3 with a standard deviation (σ) of 0.5 is applied within each iteration to remove sharp edges in the reconstructed images and render the inherently ill-posed problem more tractable. Furthermore, a non-negative constraint is applied to $a_{v,j}$ in each iteration. The relative change between $\boldsymbol{a}_v^{k+1}$ and $\boldsymbol{a}_v^k$, i.e., $\mathit{\Delta}$, is used as the termination parameter and is defined as

$$\mathit{\Delta} = \sum_{j=1}^{N} \left| a_{v,j}^{k+1} - a_{v,j}^{k} \right| \Big/ \sum_{j=1}^{N} (a_{v,j}^{k}). \tag{8}$$

The iteration stops when $\mathit{\Delta}$ is smaller than 0.1%, denoting that the convergence is reached.

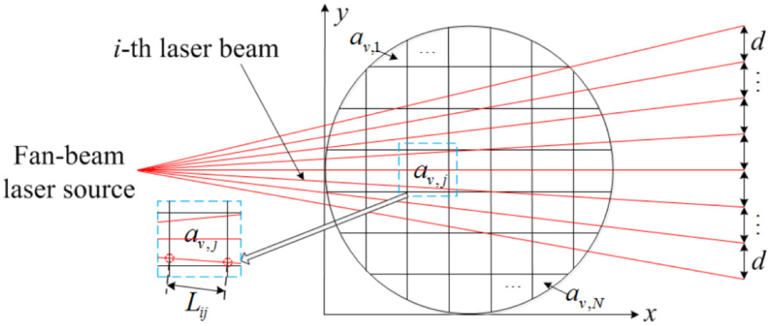

Fig. 1. Definitions of the coordinate system and the discretization configuration.

By performing the tomographic reconstructions at two pre-selected transitions (v_1 and v_2) with different temperature dependence, one can obtain the ratio of the reconstructed $a_{v_1,j}$ and $a_{v_2,j}$ in the *j*-th grid,

$$R_j = \frac{a_{v_1,j}}{a_{v_2,j}} = \frac{S_1(T_j)}{S_2(T_j)} = \frac{S_1(T_0)}{S_2(T_0)} \exp[-\frac{hc(E_1'' - E_2'')}{k}\left(\frac{1}{T_j} - \frac{1}{T_0}\right)]. \tag{9}$$

Therefore, the temperature T_j in *j*-th grid can be calculated as follows,

$$T_j = \frac{hc}{k}(E_2'' - E_1'') \Bigg/ \left[\ln\frac{a_{v_1,j}}{a_{v_2,j}} + \ln\frac{S_2(T_0)}{S_1(T_0)} + \frac{hc}{k}\frac{(E_2'' - E_1'')}{T_0} \right]. \tag{10}$$

With T_j in hand, the concentration X_j can be simultaneously obtained from Eq. (12) at the atmospheric pressure.

$$X_j = a_{v_1,j} \big/ S_1(T_j). \tag{11}$$

3. Sensor implementation

As a major product of the combustion of hydrocarbons, H_2O is selected as the target absorbing species. Two transitions of H_2O, i.e., v_1 = 7444.36 cm^{-1} and v_2 = 7185.6 cm^{-1}, are selected and can be accessed by the distributed feedback (DFB) laser diodes available in our laboratory. As noted in our previous works [26,27], good sensitivity can be ensured with the selected transitions for the temperature range in the work.

The outputs of two DFBs are first combined and then split into six channels with a fiber coupler. The output from one of the channels is directed into an etalon to monitor the frequency during the wavelength scanning, while those from the remaining channels are used to simultaneously generate five fan beams along different orientations. Figure 2 shows the schematic of the fan-beam generator. As shown in Fig. 2(a), the output from each of the five optic-fibers is firstly collimated using a collimator (CFC-5X-C, Thorlabs) and then guided through an anamorphic prism pair (PS-883-C, Thorlabs) and stretched into an elliptical beam, as shown in Fig. 2(b). In general, the cross section (perpendicular to the propagation direction z) of the collimated beam is circular with Gaussian distributed intensity along the directions of x- and y-axes. By using the anamorphic prism pair, the laser intensity along the direction of x-axis is flattened, while that along the direction of y-axis is invariant. Subsequently, the elliptical beam penetrates a cylindrical lens with a focal length of 0.58 cm (LJ1918L2-C, Thorlabs) and is transformed into a fan-shaped planar illumination. By moving a photodiode along the direction of x-axis, the intensities over the cross section of the fan-shaped planar illumination are measured with and without the anamorphic prism pair, respectively. As shown in Fig. 2(c), the horizontal coordinate is the distance between the photodiode and the center of the fan-shaped planar illumination, while the vertical coordinate is the laser intensity. It can be seen that the uniformity of the fan-shaped planar illumination is significantly improved by using the anamorphic prism pair.

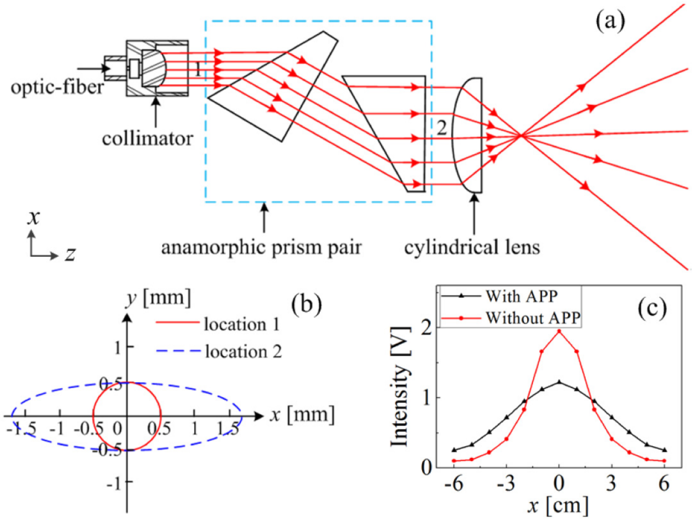

Fig. 2. Schematic of the fan-beam generator. Panel (a): the optics design. Panel (b): the circular and elliptical beam at location 1 and 2 in Panel (a). Panel (c): uniformity of the fan-shaped planar illumination obtained with and without the use of the anamorphic prism pair (APP).

#240260 Received 4 May 2015; revised 10 Aug 2015; accepted 14 Aug 2015; published 18 Aug 2015

In the TDLAS-based tomographic sensor, five fan-beam generators are placed along a circle with equal space, as shown in Fig. 3. The radii of the circle and ROI are 14 and 3 cm, respectively. The span angle of each fan-beam laser is about 24 degrees, which can effectively cover the ROI. Finally, each fan-beam laser penetrates the absorbing target and is sampled by a multi-photodiode array that contains 12 equally-spaced photodiodes (G12180-010A, Hamamatsu). Therefore, 60 ray measurements can be simultaneously obtained for each transition using parallel data acquisition instruments and used to reconstruct the distributions of temperature and H_2O concentration using the modified Landweber algorithm. It should be noted that the temporal resolution of the tomographic sensor is limited by the wavelength scanning speed of the laser diode. As the upper limit of the wavelength scanning speed the DFB laser diode adopted in this work is 10 kHz, a temporal resolution of 5 kHz can be realized with the time division multiplexing scheme [4,26,27], that is to say, 5000 frames of the tomographic images can be obtained within one second. The temporal resolution can be further increased when adopting a frequency-agile laser with a higher wavelength scanning speed. It should also be noted that the reason of using the frequency-agile laser sources in the frequency-agile tomography not only relies on improving the temporal resolution, but also on alleviating the deficiencies in spatial sampling caused by the cross parallel-beam arrangement [12–14]. In the current work, as a five-view fan-beam arrangement is adopted, the number of spatial samples is significantly larger than that in the frequency-agile tomography. In this way, the number of independent transitions can be reduced to two. Therefore, the room-temperature and narrow-linewidth laser diodes, i.e., DFB laser diodes, can be used in the experiment. Compared with the frequency-agile laser sources, the DFB laser diodes are more cost-effective and easier to be applied in laboratories and even in industries.

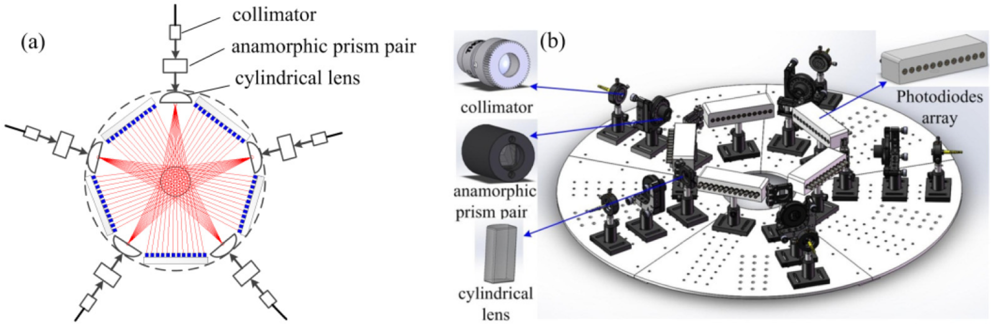

Fig. 3. (a) Schematic and (b) layout of the five-view stationary fan-beam TDLAS-based tomographic sensor.

The spatial resolution of a tomographic image can be quantified by introducing a sharp-edged target and calculating the edge spread function (ESF), as detailed in [28]. To create a sharp-edged target, the temperature in the ROI is set to be uniform, while the expected distribution of H_2O concentration in the ROI, i.e., X^{exp}, is set as a sharp-edged rectangular, as shown in Fig. 4(a). Figures 4(b) and 4(c) show the reconstructed distribution of H_2O concentration, i.e., X^{rec}, and the edge spread functions in two sampled tracks, respectively. In each track, the linear distance that covers the normalized intensity of the edge spread function from 10% to 90% is defined as the spatial resolution. As shown in Fig. 4(c), the spatial resolution in track 1 is 0.68 cm, while that in track 2 is 0.86 cm. As introduced in [28], the tracks in other regions of the ROI can be obtained by changing the annular position of the sharp-edged rectangular and repeat above simulation. By averaging the spatial resolutions in all the sampled tracks, the averaged spatial resolution of the tomographic image is obtained, which equals 0.78 cm. It should be noted that the spatial resolution obtained by using the designed fan-beam tomographic sensor is higher than those by using the parallel-beam tomographic sensor, which can be as large as several centimeters.

#240260
Received 4 May 2015; revised 10 Aug 2015; accepted 14 Aug 2015; published 18 Aug 2015

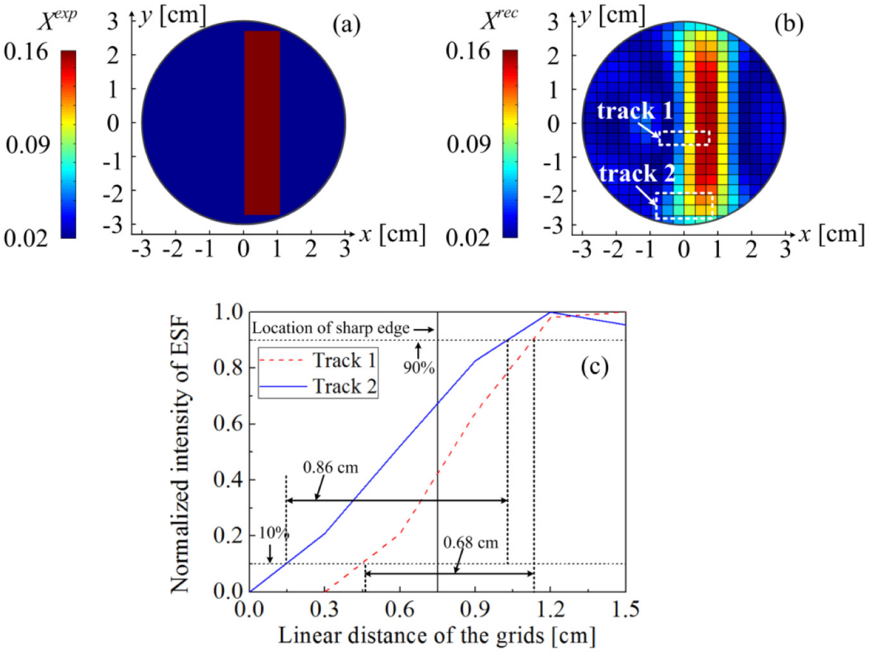

Fig. 4. Qualification of the spatial resolution of the tomographic image. Panel (a): expected distribution of H_2O concentration with a rectangular sharp-edged feature. Panel (b): the reconstructed distribution of H_2O concentration and two sampled tracks to calculate the spatial resolution. Panel (c): edge spread functions and corresponding spatial resolution in the two sampled tracks.

The TDLAS-based tomographic sensor designed in this work features three significant advantages. First, the sensor bases on a stationary fan-beam arrangement, by which a high spatial resolution is guaranteed because the distance between two neighboring detectors on the multi-photodiode array is reduced to about the size of a photodiode. Second, instead of rotating the illuminating beams or translating the target, the fan-beam illuminations from five views are simultaneously generated, and hence TDLAS data from the five views can be simultaneously measured. Therefore, the stationary tomographic sensor not only significantly increases the temporal resolution, but also greatly reduces the uncertainty introduced by the mechanical movements and greatly improves the reliability. Third, the novel optics design with the combination of anamorphic prism pair and cylindrical lens also greatly improves the uniformity of the fan-shaped planar illumination, and hence improves the reconstruction fidelity.

4. Results and discussions

4.1 Numerical validation

To validate the geometrical design of the TDLAS sensor, numerical simulation was firstly carried out. In the simulation, the asymmetric phantoms of temperature, i.e., T^{exp}, and H_2O concentration, i.e., X^{exp}, were created, as depicted in Figs. 5(a) and 5(b), respectively. The origin of the *xOy* coordinate system is at the center of the tomographic area with a radius of 3 cm. In a hydrocarbon flame, the H_2O concentration is generally well-correlated with the temperature. Therefore, to evaluate the performance of the sensor on reconstructing multimodal distributions, both T^{exp} and X^{exp}, each consisting of two inhomogeneities with different peak values at (0.8, 0.8) and (−1, −1), are simulated, respectively. The gradients of the inhomogeneities in the phantoms are different from each other along the directions of *x*- and *y*-axes. By applying the fan-beam arrangements in the sensor to the forward problem in

Eq. (5), the noise-free projections, i.e., the vector of $\boldsymbol{A}_v$, were obtained. As shown by Fig. 6, distributions of temperature and H_2O concentration, noted as T^{rec} and X^{rec}, were simultaneously reconstructed by using the modified Landweber algorithm. It can be seen that the tomographic images agree well with the phantoms.

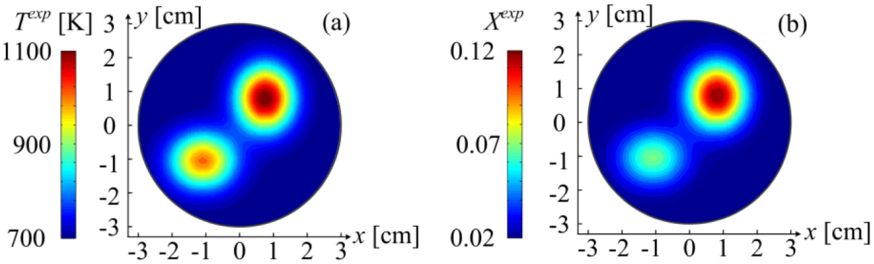

Fig. 5. Phantoms of asymmetric distributions of (a) temperature and (b) H2O concentration in the simulation.

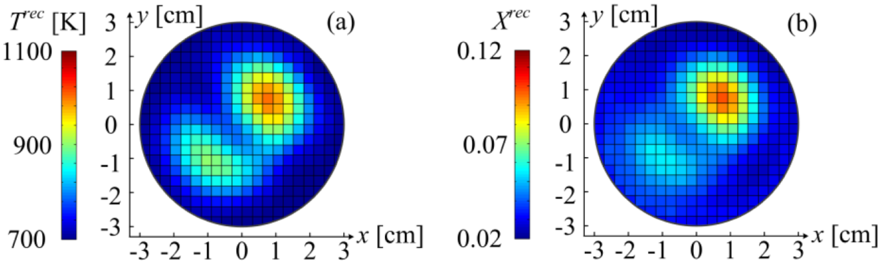

Fig. 6. Reconstructed distributions of (a) temperature and (b) H_2O concentration with noise-free projections in the simulation.

To compare the tomographic images with the phantoms, each of the phantoms is discretized into N_p grids (N_p = 1876 in this case), which results in a spacing of 0.12 cm between the neighboring grids along both the directions of x- and y-axes. When comparing a lower resolution reconstruction (with N grids) to a higher spatially resolved "true" distribution (the phantom, with N_p grids), the tomographic image with N grids is interpolated into an image with N_p grids using the nearest neighbor interpolation. In this way, the same discretization is imposed on the tomographic image and the phantom. Then, to numerically evaluate the accuracy of the tomographic images, the average normalized differences between the tomographic images and the phantoms are defined as

$$c_T = \sum_{j=1}^{N_p} \left(\left| T_j^{rec} - T_j^{exp} \right| \Big/ T_j^{exp} \right) \Bigg/ N_p \,, \tag{12}$$

$$c_X = \sum_{j=1}^{N_p} \left(\left| X_j^{rec} - X_j^{exp} \right| \Big/ X_j^{exp} \right) \Bigg/ N_p \,, \tag{13}$$

where c_T and c_X denote the average normalized differences between the reconstructed distributions of temperature and H_2O concentration and those in the corresponding phantom, respectively. With the same numbers of views and laser beams in each view, c_T and c_X are dependent on N. As shown in Fig. 7, both c_T and c_X are the smallest for an optimum N, noted as N_{opt}. Both c_T and c_X increase when N decreases or increases from N_{opt}, denoting that the tomographic images gradually depart from the phantoms.

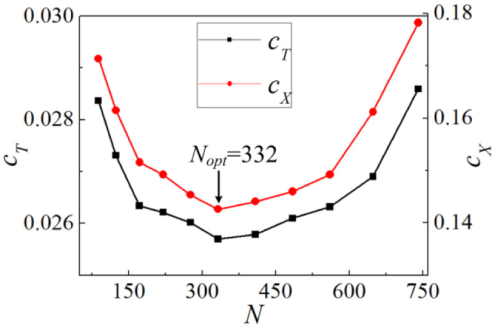

Fig. 7. Dependence of c_T and c_X on the number of grids with the designed tomographic sensor.

Figure 8 shows the temperature distribution reconstructed when N equals 124, 332 and 560, respectively. When N equals 124, the tomographic image of temperature distribution is too rough to describe the phantom in Fig. 5(a). When N equals 560, although the tomographic image is capable of capturing more details, some artifacts exist in the tomographic image because the solution is more ill-posed caused by the increasing number of analytes to be obtained. Therefore, N is selected as 332 to balance the reserved details against the accuracy of the tomographic image.

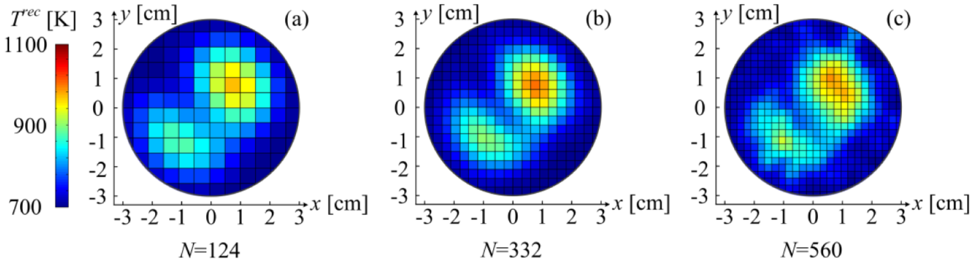

Fig. 8. Reconstructed temperature distributions with noise-free projections when the number of grids equals (a) 124, (b) 332 and (c) 560, respectively.

Although larger numbers of views, noted as N_v, and the laser beams in each view, noted as N_l, will contribute to improving the accuracy of the tomographic reconstruction, they will also make the optics of the tomographic sensor more complicated and harder to realize. As illustrated in Table 1 and Table 2, for a fixed number of laser beams in each view, the relative changes of c_T and c_X between 3 and 5 views are larger than 35%, while those between 5 and 7 views are about 15%. It can be seen that a significant improvement of the tomographic accuracy can be obtained by increasing the number of views from 3 to 5. Furthermore, for a fixed number of views, c_T and c_X decreases to a larger extent if the numbers of laser beams in each view increases from 8 to 10, or from 10 to 12, while it decreases to a smaller extent if the number of laser beams is larger than 12. Therefore, to balance the tomographic accuracy and the complexity of optics of the tomographic sensor, the numbers of views and the laser beams in each view are selected as 5 and 12, respectively.

Table 1. Dependence of c_T on the number of views, noted as N_v, and the number of laser beams in each view, noted as N_l.

N_v	$N_l = 8$	$N_l = 10$	$N_l = 12$	$N_l = 14$	$N_l = 16$
3	4.46%	4.25%	4.13%	4.09%	4.07%
5	2.85%	2.69%	2.57%	2.55%	2.52%
7	2.46%	2.38%	2.28%	2.24%	2.22%

#240260
Received 4 May 2015; revised 10 Aug 2015; accepted 14 Aug 2015; published 18 Aug 2015

Table 2. Dependence of c_X on the number of views, noted as N_v, and the number of laser beams in each view, noted as N_l.

N_v	$N_l = 8$	$N_l = 10$	$N_l = 12$	$N_l = 14$	$N_l = 16$
3	24.82%	23.79%	23.30%	22.75%	22.63%
5	15.77%	14.96%	14.26%	14.14%	14.01%
7	13.66%	13.22%	12.65%	12.33%	12.28%

To further validate the modified Landweber algorithm, it is compared with two well-known limited view tomography algorithms [29,30], i.e., the algebraic reconstruction technique (ART) and the simultaneous multiplicative ART (SMART). Here, the performance of an algorithm is evaluated by calculating c_T and the convergence time. As listed in Table 3, c_T obtained using the modified Landweber algorithm and the SMART are significantly smaller than that obtained using the ART, denoting that the tomographic images reconstructed using the modified Landweber algorithm and the SMART are more accurate. Furthermore, although c_T obtained using the SMART are slightly smaller than that obtained using the modified Landweber algorithm, the convergence time for the SMART is more than triple time needed for the modified Landweber algorithm. Therefore, to make a trade-off between the accuracy and the real time performance of the algorithm, the modified Landweber algorithm is selected in this work. It should also be noted that this work aims to develop a fan-beam TDLAS-based tomographic sensor with both high spatial and temporal resolutions. We focus more on designing the optics of the tomographic sensor to improve the spatial and temporal resolutions instead of developing new tomographic algorithms. More algorithms will be implemented to improve the performance of the system in the future.

Table 3. List of values of c_T and convergence time of the modified Landweber algorithm, ART and SMART, respectively.

Algorithms	c_T	Convergence time [s]
Modified Landweber	2.57%	0.127
ART	3.17%	0.836
SMART	2.49%	0.393

In practical measurements, the projections are contaminated with noises. To evaluate the accuracy and robustness of tomography at different noise levels, T^{rec} and X^{rec} were retrieved by adding 0.1% to 5% random noises on the noise-free vector $\boldsymbol{A}_v$. The noise at a relatively lower level, i.e., 0.1%, represents the situation where the projections are subject to the fundamental noises, i.e., shot noise, detector noise, etc., while the noise at a relatively higher level, i.e., 5%, represents the situation where the projections are also subject to flow-induced noises mainly caused by beam steering and particulate scattering. At each noise level, 100 repetitive simulations were carried out, and both the mean values of 100 c_T and c_X and their standard deviations were calculated. As shown in Fig. 9, the midpoints signify the mean values of c_T and c_X, while the error bars to each midpoint denote their standard deviation. In the noise-free cases, the mean values of c_T and c_X equal 2.57% and 14.26% respectively. The maximum, minimum and root-mean-square values of $\left|T_j^{rec} - T_j^{exp}\right| / T_j^{exp}$ equal 0.146, 2.35×10^{-4} and 0.044, while those of $\left|X_j^{rec} - X_j^{exp}\right| / X_j^{exp}$ equal 0.515, 3.38×10^{-4} and 0.206, respectively. It should be noted that the values of c_X are relatively large because the absolute value of the H_2O concentration is relatively small. To make this point clearer, $\left|T_j^{rec} - T_j^{exp}\right|$ and $\left|X_j^{rec} - X_j^{exp}\right|$ are also calculated in the noise-free case, respectively. The maximum, minimum and root-mean-square values for $\left|T_j^{rec} - T_j^{exp}\right|$ equal 149 K, 6 K and 34.6 K, while those of $\left|X_j^{rec} - X_j^{exp}\right|$ equal 3.65×10^{-2}, 1.21×10^{-6} and 8.7×10^{-3}, respectively. Although the values of $\left|X_j^{rec} - X_j^{exp}\right|$ are very small, those of $\left|X_j^{rec} - X_j^{exp}\right| / X_j^{exp}$ are magnified because the absolute value of the H_2O concentration is smaller than 0.15. The values of

$\left|X_j^{rec} - X_j^{exp}\right| / X_j^{exp}$ are more significantly magnified in case of a much smaller X_j^{exp}. When the random noise that added on the projections increases from 0.1% to 1%, the maximum relative changes of the mean values of c_T and c_X are smaller than 1.75% and 0.14%, respectively. In addition, the maximum standard deviations of c_T and c_X for above cases are smaller than 7.95×10^{-4} and 7.98×10^{-4}, respectively. When the noise level reaches 5%, the mean values of c_T and c_X increase to 3.15% and 14.58%, while the standard deviations of c_T and c_X increase to 2.34×10^{-3} and 2.85×10^{-3}. It can be seen that accurate and stable solutions of T^{rec} and X^{rec} can be obtained when the random noise is less than 1%. Both the mean values and standard deviations of the c_T and c_X increase for a higher level of random noise, denoting that the tomographic images deviate from the phantoms to a larger extent. Although the tomographic images reconstructed using the noise-contaminated data are less accurate than those with the noise-free data, the tomographic images can still effectively locate the inhomogeneities and capture the magnitude of the phantoms even with 5% random noise added to the projections, as shown in Fig. 10.

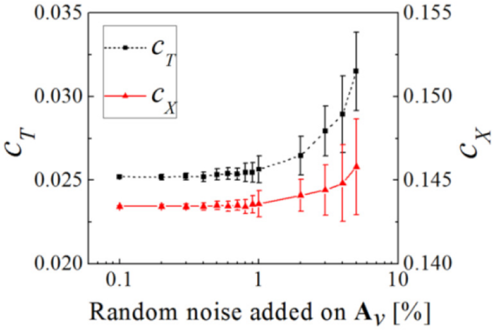

Fig. 9. Evaluation of the accuracy and robustness of the fan-beam TDLAS-based tomography sensor at different noise levels.

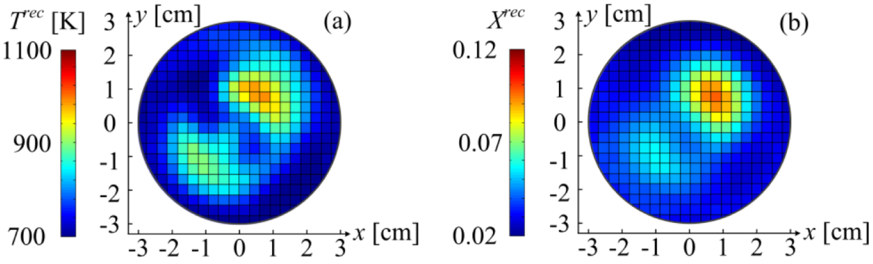

Fig. 10. Reconstructed distributions of (a) temperature and (b) H_2O concentration with 5% random noise adding on the noise-free projections in the simulation.

4.2 Experimental results

In the experiment, the flame was generated by using a McKenna flat flame burner. By setting the flow rates of methane and air to 1.2 and 15.25 L/min, an equivalence of 0.749 was obtained. To reduce the impact of convection between the core flame and the surrounding air, shrouding nitrogen was released around the burner plug. As detailed in [31], the flow rate of the shrouding nitrogen was set to 22.5 L/min to match the velocity of the fuel. The original point of the *xOy* coordinate system is at the center of the tomographic area with a radius of 3 cm. The height above the burner plug is noted as *z*. The height of the fan-beam illumination was adjusted to 3 cm above the burner plug, that is, the cross section of the flame at $z = 3$ cm was selected as the absorbing target in the ROI. As shown in Fig. 11, the radius of the cross section of the flame at $z = 3$ cm is smaller than the radius of the burner plug that equals 3 cm. Therefore, the ROI with a radius of 3 cm is sufficient to cover the cross section of the flame.

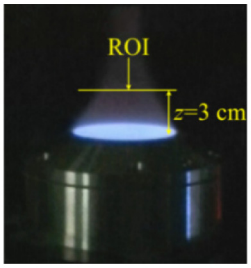

Fig. 11. Flame generated by using a McKenna flat flame burner. In the experiment, the flow rates of methane, air and shrouding nitrogen were set to 1.2, 15.25 and 22.5 L/min, respectively.

The data acquisition rate is 2.5 Msps for each measurement channel to sample the transmitted laser intensity. The transmitted laser intensities obtained by the 60 photodiodes were sequentially sampled by a multiplexing circuit. The wavelength scanning speed of each of the two DFB laser diodes was 10 kHz, and hence the scanning period was 0.2 ms (2/10 kHz) with the time division multiplexing scheme. Therefore, it took 12 ms to obtain the 60 projections that are used to reconstruct one frame of tomographic image. Because the premixed flame in this work is laminar and relatively stable, and the tomographic image updates every 12 ms, the imaging speed is fast enough to monitor the distributions of temperature and H_2O concentration in the combustion process. For violently turbulent flows, parallel data acquisition instruments can be employed to further increase the temporal resolution, as noted in section 3.

To assess the performance of the tomographic sensor, the distributions of temperature and H_2O concentration of the premixed flame are reconstructed, as shown in Figs. 12(a) and 12(b), respectively. The edges of the reconstructed distributions of temperature and H_2O concentration are clearly depicted, denoting that the circular ROI completely covers the cross section of the flame. In order to obtain a larger size of the reconstructed domain, we can enlarge the span angle of the fan-beam illumination with the same or increased number of ray measurements in each view. If we use the same number of ray measurements in each view, we will have to increase the distance between the neighboring photodiodes on the multi-photodiode array. However, this will decrease the spatial resolution of the tomographic images. If the distance between the neighboring photodiodes on the multi-photodiode array remains unchanged, more photodiodes, and hence more ray measurements should be added in order to detect the fan-beam illumination within the enlarged span angle. Therefore, the span angle and the area of the ROI should be chosen according to the size of the flame. For a flame with larger size, the span angle of the fan-beam illumination can be enlarged by choosing a cylindrical lens with a smaller focal length and extending the width of the multi-photodiode array. In the core flame, T^{rec} and X^{rec} are uniform, and equal 1346 K and 0.138, respectively. The expected H_2O concentration, i.e., X^{exp}, in the core flame at the equivalence of 0.749 can be obtained by using equilibrium calculations, which equals 0.146. Therefore, the relative error between X^{rec} and X^{exp} is 5.48%, denoting that the tomographic sensor can be used to obtain the H_2O concentration distributions. At the boundary of the flame, T^{rec} and X^{rec} gradually decrease to surrounding values because of heat transfer and gas mixing between the combustion products and the shrouding nitrogen.

#240260 Received 4 May 2015; revised 10 Aug 2015; accepted 14 Aug 2015; published 18 Aug 2015

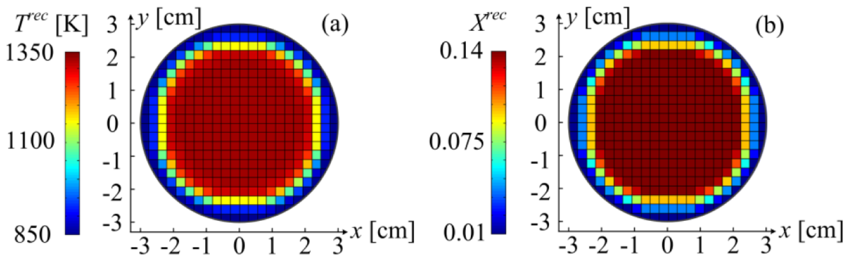

Fig. 12. Reconstructed distributions of (a) temperature and (b) H_2O concentration at the height of 3 cm above the burner plug when the equivalence was set to 0.749.

Furthermore, 100 repetitive measurements were performed to evaluate the variation in the tomographic images over many measurement periods. In each grid, the values of temperature and H_2O concentration from 100 measurements are averaged. Therefore, we obtain the averaged tomographic images of T^{rec} and X^{rec} from 100 measurements, noted as T^{M_rec} and X^{M_rec}, respectively. The average normalized difference between T^{rec} and T^{M_rec}, noted as e_T, is defined as,

$$e_T = \sum_{j=1}^{N} \left(\left| T_j^{rec} - T_j^{M\_rec} \right| \Big/ T_j^{M\_rec} \right) \Big/ N, \tag{14}$$

and the average normalized difference between X^{rec} and X^{M_rec}, noted as e_X, is defined as,

$$e_X = \sum_{j=1}^{N} \left(\left| X_j^{rec} - X_j^{M\_rec} \right| \Big/ X_j^{M\_rec} \right) \Big/ N, \tag{15}$$

The variability in the tomographic images is therefore quantitatively described by the standard deviations of e_T and e_X obtained from 100 measurements, noted as, σ_T and σ_X, respectively. In this case, σ_T and σ_X equal 1.13×10^{-3} and 9.64×10^{-4}, respectively.

The fluctuations of the tomographic images are mainly caused by the noises in the projections. The fundamental noises that mainly contain shot noise and detector noise can be measured in existence of the flame, while the larger flow-induced noises that mainly caused by beam steering and particulate scattering can be evaluated with a stable flame. In the experiment, the TDLAS data for two transitions at $v_1 = 7444.36$ cm^{-1} and $v_2 = 7185.6$ cm^{-1} are measured for 100 times with the premixed flame in room air, respectively. Figure 13 shows the TDLAS data sampled by a photodiode for the two cases. The midpoints denote the mean values of the repetitively sampled TDLAS data, while the error bars to each midpoint signify their standard deviations. For each of the transitions, the standard deviations obtained in room air are significantly smaller than those obtained in the premixed flame. The results show that the magnitudes of fundamental noises are much smaller than flow-induced noises.

It is worth mentioning that, although the use of the fan-beam arrangement and the designed multi-photodiode array reduces the distance between two neighboring detectors and contributes to improving the spatial resolution, the majority of the optical power falls between the neighboring detectors and hence is lost. Given the power of the output laser, the transmitted laser intensity obtained by the photodiode with the fan-beam arrangement is significantly smaller than that with the parallel-beam arrangement. Therefore, the photoelectric detecting circuits and data acquisition instruments should be of higher amplification factor and with a sufficiently high signal to noise ratio (SNR). To quantitatively evaluate the sensor performance, the SNR of the TDLAS data sampled in the premixed flame is calculated. In this case, the SNR is influenced by both fundamental and flow-induced noises. For the transitions at $v_1 = 7444.36$ cm^{-1} and $v_2 = 7185.6$ cm^{-1}, the SNRs equal 40.2 dB and 44.8 dB, respectively, implying that the noise level is smaller than 1% of the magnitude

#240260
© 2015 OSA
Received 4 May 2015; revised 10 Aug 2015; accepted 14 Aug 2015; published 18 Aug 2015

of the signal. The tomographic images reconstructed from the measured data, as shown in subsection 4.1 show that the SNR of the sensor is high enough to obtain reliable data for reconstructing tomographic images of the flame.

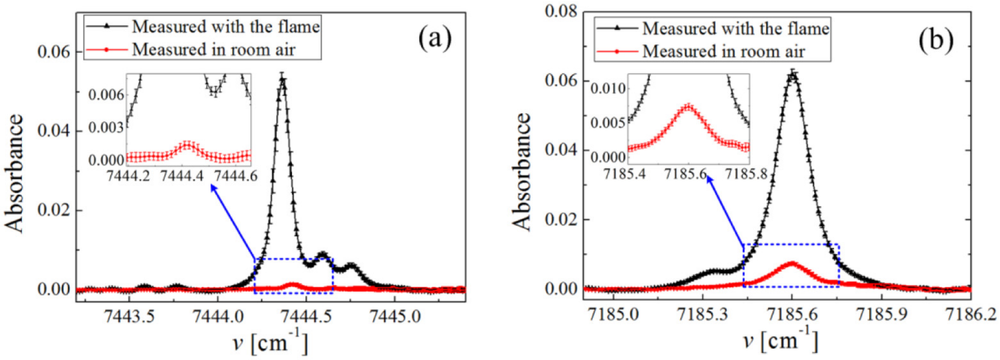

Fig. 13. Sampled TDLAS data obtained by a photodiode in room air and in the premixed flame for transitions at (a) v_1 = 7444.36 cm^{-1} and (b) v_2 = 7185.6 cm^{-1}, respectively.

To generate various flame profiles, one or two rectangular steel cubes with different sizes were put on different positions of the burner. Firstly, a cube was put on the center of the burner plug. The length, width and height of the cube are 2 cm, 2 cm and 2 cm, respectively. As shown in Figs. 14(a) and 14(b), D_1 is the region that the cube occupies on the burner plug. The ROI is still located at 3 cm above the burner plug. With the projections in hand, two-dimensional distributions of temperature, i.e., T^{rec}, and H_2O concentration, i.e., X^{rec}, were reconstructed using the modified Landweber algorithm, respectively. Due to the blocking of the steel cube of the gaseous flow and heat loss, a low-temperature area is captured in the center of the ROI, as shown in Fig. 14(c). Although region D_1 is rectangular and sharp-edged, the low-temperature area in the tomographic image looks approximately circular and smooth-edged. On one hand, the premixed flame generates high-temperature gaseous mixture flowing upwards. When the gaseous mixture flows over the blocking cube, the mixture quickly flows into the blocked area above the cube, generating flow turbulence. The flow turbulence and heat transfer not only smooth the four corners of the low-temperature area, but also smooth its boundary. On the other hand, as illustrated in section 3, the average spatial resolution is as low as 0.78 cm, which intensified the smoothness of the sharp edge of region D_1 in the tomographic image to some extent. Furthermore, as the combustion is complete in this case, the H_2O concentration on the cross section of the premixed flame is uniform. As shown in Fig. 14(d), X^{rec} is uniform and equals 0.136 in the core flame, while X^{rec} gradually decreases due to gas mixing between the combustion products and the shrouding nitrogen at the boundary of the flame.

For the second case, the cube was put on one side of the burner plug. The length, width and height of the cube are 1 cm, 1 cm and 2 cm, respectively. As shown in Figs. 15(a) and 15(b), D_2 is the region that the cube occupies on the burner plug. The tomographic images in Figs. 15(c) and 15(d) show that T^{rec} in region D_2 is much lower than that in the nearby region due to the heat loss to the steel cube, while X^{rec} is uniform and equals 0.136 in the core flame.

#240260 Received 4 May 2015; revised 10 Aug 2015; accepted 14 Aug 2015; published 18 Aug 2015

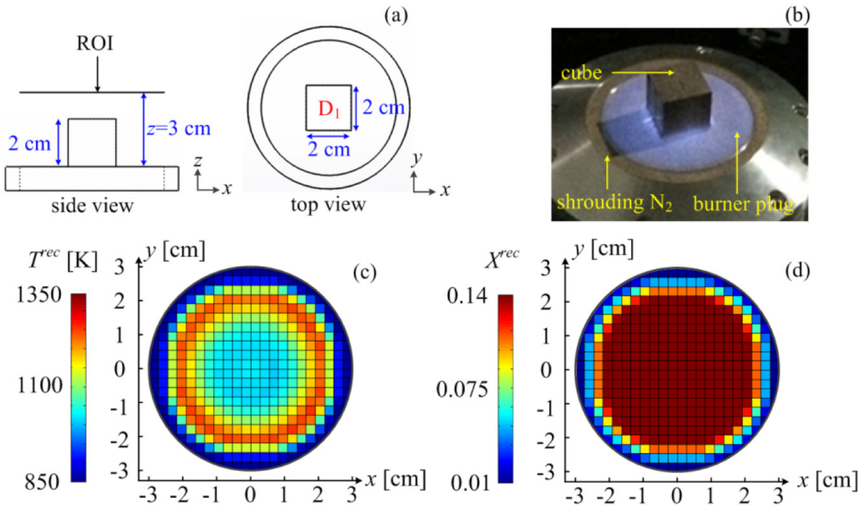

Fig. 14. Experimental setup and tomographic results by putting a cube on the center of the burner plug. Panel (a) and Panel (b) show the schematic diagram and photo of the experimental setup, respectively. Panel (c) and Panel (d) show the reconstructed distributions of temperature and H_2O concentrations, respectively.

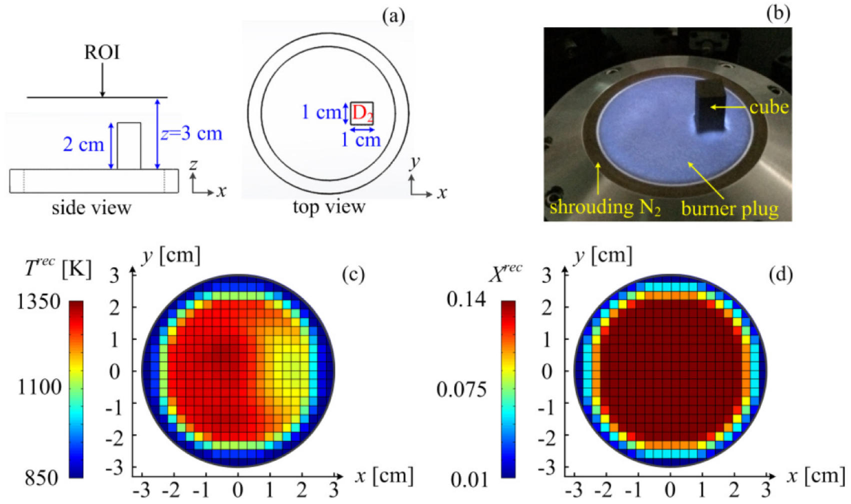

Fig. 15. Experimental setup and tomographic results by putting a cube on one side of the burner plug. Panel (a) and Panel (b) show the schematic diagram and photo of the experimental setup, respectively. Panel (c) and Panel (d) show the reconstructed distributions of temperature and H_2O concentrations, respectively.

To create a more complex flame profile, two cubes were put on the burner plug in region D_3 and region D_4, as shown in Figs. 16(a) and 16(b), respectively. The length, width and height of the cube in the region D_3 are 1 cm, 1 cm and 1 cm, while those of the cube in region D_4 are 1 cm, 3 cm and 2 cm, respectively. As shown in Fig. 16(c), T^{rec} in region D_3 and region D_4 are lower than those in the central region without the cubes. As the top of the cube in region D_4 is closer to the ROI compared with that in region D_3, more heat of the flow transfers to the cube in region D_4. Furthermore, the gaseous mixture flows over the cubes and diffuses to a larger extent in the region D_3 than that in region D_4 at the height of z = 3 cm, which contributes to more sufficient gaseous mixture and hence releasing more heat in region D_3. Therefore, T^{rec} in region D_3 is higher than that in region D_4. Furthermore, because the cube in region D_4 is close to the boundary of the burner plug, the flow disturbance mixes the shrouding nitrogen into the flame, leading to lower H_2O concentration than its nominal value, as shown in Fig. 16(d).

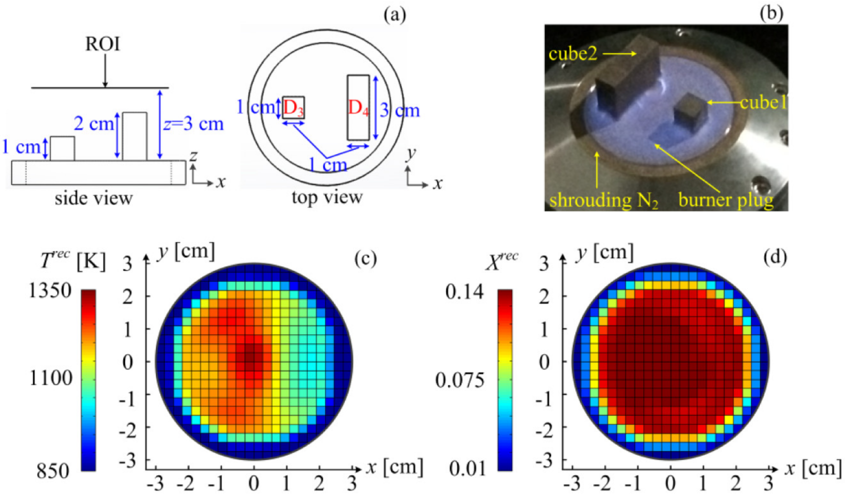

Fig. 16. Experimental setup and tomographic results by putting two cubes on the burner plug. Panel (a) and Panel (b) show the schematic diagram and photo of the experimental setup, respectively. Panel (c) and Panel (d) show the reconstructed distributions of temperature and H_2O concentrations, respectively.

5. Summary

A stationary fan-beam TDLAS sensor was developed for high-speed and simultaneous tomographic imaging of temperature and gas concentration. The use of fan-beam arrangement and the designed multi-photodiode array approximately reduce the distance between two neighboring detectors in a view to size of a photodiode, and hence improve the spatial resolution to 0.78 cm. By combining anamorphic prism pair with cylindrical lens, the uniformity of the fan-shaped planar laser illumination and hence the reconstruction fidelity are significantly improved. The design of the sensor that simultaneously generates five-view fan-beam illumination not only improves the temporal resolution of image reconstruction, but also reduces the uncertainty introduced by mechanical movements of either the sensor or the object. When adopting parallel data acquisition instruments, a temporal resolution of 5 kHz can be realized by the time division multiplexing scheme when each of the two DFB laser diodes is scanned by 10 kHz. The modified Landweber algorithm is employed to obtain the tomographic images of temperature and gas concentration.

Simulation on multimodal phantoms of temperature and H_2O concentration show that the tomographic images can reflect the shape and magnitude of the phantoms for noise-free projections and noise-contaminated projections with noise level below 5%. In the experiment, the sensor was firstly validated by imaging the distributions of temperature and H_2O concentration in a premixed flame generated by the McKenna flat flame burner. Then, experiments with various flame profiles show that the reconstructed distributions of the temperature and the H_2O concentration agree well with the expected distributions, denoting that the sensor is effective for combustion flame monitoring.

Acknowledgments

The authors gratefully acknowledge the financial support by the National Science Foundation of China (Grant No. 61225006, Grant No. 61327011), Fundamental Research Funds for the

Central Universities (Grant No. 30471501) and Program for Changjiang Scholars and Innovative Research Team in University (IRT1203).